Desalination and Water Treatment
www.deswater.com

doi: 10.5004/dwt.2019.24413

163 (2019) 243–259
September

A series of novel non-stoichiometric cobalt ferrite nanoparticles as efficient reusable nanoadsorbents for hexachromium ions

Lotfi Ben Tahar[a,b,c,*], Mohamed Habib Oueslati[a,d], Sofien Saidani[b,e], Agnès Smith[e]

[a]*College of Science of Arar, Northern Border University, P.O. Box 1231, Arar 91431, Saudi Arabia, Tel. +966 50 00 88 65 85/+216 98 902 376; emails: bentaharlotfi@gmail.com/lotfi.taher@nbu.edu.sa (L. Ben Tahar), ouesmed74@gmail.com (M.H. Oueslati)*
[b]*Faculté des Sciences de Bizerte, Université de Carthage, LR18 ES11, Laboratoire des composés hétéro-organiques et des matériaux nanostructurés, 7021, Zarzouna, Tunisia, email: sofien.saidani@unilim.fr*
[c]*Faculté des Sciences de Tunis, Université de Tunis El Manar, Campus Universitaire, 2092, Tunisia*
[d]*Department of Chemistry, Preparatory Institute for Scientific and Technical Studies, Carthage University, P.O. Box 51, La Marsa 2070, Tunisia*
[e]*Institute of Research on Ceramics, IRCER - UMR CNRS 7315, Université de Limoges, Centre Européen de la Céramique, 12 rue Atlantis, 87068 Limoges cedex, France, email: agnes.smith@unilim.fr*

Received 30 December 2019; Accepted 14 May 2019

ABSTRACT

A series of novel four non-stoichiometric cobalt ferrite nanoparticles (NPs) with the chemical composition, $Co_x^{2+}Fe_{\frac{8-2x}{3}}^{3+}V_{\frac{1-x}{3}}O_4$ (x ~ 0.2, 0.4, 0.6, 1.0, V = vacancy) was synthesized by the polyol method. The produced NPs were systematically characterized and studied by several techniques including X-ray diffraction, energy dispersive X-ray, infrared spectroscopy, thermal analysis, transmission electron microscopy and SQUID magnetometry for their chemical composition, structure, microstructure, surface chemistry and magnetic properties. The nanosized particles (~5–7 nm) are roughly spherical in shape and exhibiting superparamagnetic behavior with a reasonable saturation magnetization and a high Curie temperature. Additionally, the thermal stability of the NPs was studied, and a decomposition reaction scheme was proposed. The effects of various physicochemical parameters, such as the initial Cr(VI) concentration, the NPs dosage, the contact time and the commonly coexisting ions in wastewaters (Ba^{2+}, Pb^{2+}, Zn^{2+}, Cl^-, SO_4^{2-}, PO_4^{3-},…), on the removal efficiency of Cr(VI) by low-temperature calcined NPs was studied at pH ~ 2.0. The best removal efficiency was found with the two nanoferrites with the composition x ~ 0.6 and ~1.0. Their respective adsorption capacity calculated from the Langmuir isothermal model for an adsorbent dosage of 4.0 g L^{-1}, were ~17.0 and ~13.0 mg g^{-1}. Besides, for an industrial, economic and environmental purpose, the reusability efficiency of the NPs was tested for seven adsorption–desorption–regeneration cycles.

Keywords: Nanoparticle; Cobalt ferrite; Superparamagnetism; Adsorption; Chromium; Reusability; Coexisting ions

1. Introduction

The problem of water pollution is jeopardizing our health, the aquatic system, as well as the social and economic development [1]. Contamination of different classes of water (surface water, groundwater, etc.) is a serious problem worldwide caused by the rapid population growth and industrial expansion as well as global environmental change [2]. Further, due to lifestyle changes, new non-degradable micropollutants with serious environmental risk called

* Corresponding author.

"contaminants of emerging concern" complicate the water pollution problem [3]. Pesticides, pharmaceuticals and personal care products are the most hazardous contaminants among many others. Consequently, the quantity of wastewater produced, and its overall pollution load are continuously increasing worldwide, especially in industrialized countries. According to the United Nations, more than 80% of the world's wastewater flows back into the environment without being treated [4]. All these causes render the conventional methods (coagulation–flocculation, chemical precipitation, ion exchange, adsorption, membrane filtration, electrochemistry) incapable to satisfy the huge demands for water treatment. Additionally, the traditional methods suffer from several limitations such as incomplete pollutant removal (and consequently the incapability for meeting minimum safety standards for specific reclamation purpose), time and energy consuming (and consequently high operational cost), low selectivity, release of huge amounts of sludge and the difficulty of recycling [5,6]. In many treatments, the sludges are themselves harmful which causes disposal problem and thus increases the operation cost [6]. This has led to extensive research of advanced technologies that can overcome such inherent limitations.

Nanotechnology promises to not only overcome major challenges faced by existing treatment technologies but also to provide new treatment capabilities that could allow economic utilization of unconventional water sources to expand the water supply [5,7,8]. Adsorption and electrocatalytic oxidation/reduction on selected nanomaterials such as metallic and oxide-based NPs are reported to be the most promising methods for the purpose, particularly, for the remediation of the environment from the highly hazardous chemical species such as the emerging contaminants and the persistent organic pollutants [8,9]. Taking advantages of its simplicity, selectivity and relevancy to the industrial application, nanoadsorption has recently become the major focus of numerous investigations. The main features of the emerging technology is that it can be used for the removal and/or reduction and preconcentration of various hazardous species (heavy metals, dyes) by simply tuning the adsorbent nature and some physico-chemical parameters [2,5]. In the last few decades, numerous materials (activated carbon, silica gel, zeolites, metals, metal oxides, bioadsorbents,…) have been examined for their potential in the adsorption of diverse types of contaminated aqueous systems [5,10].

The magnetic iron oxide NPs with the spinel-like structure ($M^{(II)}Fe_2^{(III)}O_4$, where M = Fe, Cu, Ni, Co, Mn) including the Fe(II)-deficient magnetite (γ-Fe_2O_3), revealed to be excellent candidates for the removal of various contaminants as well as catalyst for degradation of organic water pollutants [2,5,11]. Their superiority is related to a number of exceptional advantages such as the low-cost and the ease of processing synthesis, the high specific area, the surface modifiability (and thus good dispersion ability, enhanced removability and affinity toward target species), the tuned magnetic properties (and thus ease of separation by applying an external magnetic field) and the high recyclability (and thus industrial applicability) [11]. The use of magnetic NPs has gained special attention as adsorbent agents of hazardous heavy metal species from wastewaters [11]. The most effective factors in an adsorption process are the particle microstructure (mean particle size and shape) and the pH of the aqueous medium. The last factor could affect the surface charge, degree of ionization and species distribution of both adsorbent and adsorbate. The pH of maximum removal capacity on bare and functionalized NPs is heavy metal type–dependent. It is of about 2–3 for the removal of Cr(VI) [9,12], in the range ~2–6.5 for the removal of As(III) and As(V) [6,13], and in the range ~4–6 for the removal of M(II) (M = Pb, Cu, Zn, Cd) [14].

Aiming to elaborate efficient spinel–type NPs for the removal of hazardous chemical species, we recently undertook a systematic research work by changing various parameters including the NPs nature, the NPs size via varying a number of physicochemical parameters. Adopting the polyol method for the synthesis of the NPs, we began by the chemical preparation of the simplest members (magnetite and maghemite and their solid solution) of the spinel-type ferrite class and then studied their efficiency for the removal of hexachromium entities at the optimum pH ~2.0 [15]. For the maghemite NPs, we found an encouraging result with a maximum adsorption capacity of 12.5 mg g^{-1} NPs for an adsorbent dosage of 4.0 g L^{-1}. Further, with the kind of NPs, we have successfully reduced Cr(VI) concentration to about 80%–100% in less than 1 h starting from solutions with initial Cr(VI) concentration in the range 20–80 mg L^{-1}. Unfortunately, the NPs were not chemically stable enough, thus limiting their reusability. In acidic medium, they gradually decomposed and finished by losing their removal ability as well as their magnetic properties. For these reasons, we recently synthesized very fine powder with a mean particle size of ~10 nm of a new cobalt–zinc ferrite with good magnetic features and particularly with a high chemical stability [16]. These advantages, compared with magnetite and maghemite, have permitted fast removal of Cr(VI) species with a significant increase in the removal capacity (≈16.0 mg g^{-1}). Additionally, the NPs have showed good chemical stability, thus allowing an important number of adsorption–desorption–regeneration cycles without any significant loss in sorption capacity.

In the present research work, we report the synthesis of a series of new non-stoichiometric cobalt ferrite NPs using the polyol method. The NPs were systematically characterized by X-ray diffraction (XRD), infrared spectroscopy (IR), thermal analysis (TG/DTA), energy dispersive X-ray (EDX), transmission electron microscopy (TEM) and SQUID magnetometry. Then, a detailed study of the Cr(VI) removal efficiency on the produced NPs as well as their reusability was carried out at pH ~ 2.0 as a function of the NPs nature, the NPs dose, the contact time and the type of the coexisting ion. The obtained results were interpreted and compared with those reported in the literature for similar materials.

2. Experimental procedure

2.1. Nanoparticles synthesis

The experimental part was initially aimed to produce the mixed CoZn ferrites NPs with the nominal composition, $Co_xZn_{1-x}Fe_2O_4$ (x = 0.2, 0.4, 0.6, 1.0). The precursor salts, $Zn(CH_3CO_2)_2{\cdot}2H_2O$ (Acros, Geel, Belgium, >98%), $Co(CH_3CO_2)_2{\cdot}4H_2O$ (Acros, Geel, Belgium, 97%), and $FeCl_3$

(Sigma-Aldrich, St. Louis, USA), 97%) and sodium acetate trihydrate (Sigma-Aldrich, St. Louis, USA, 99%) were accurately weighted according to their stoichiometry. The chemicals were then dissolved in 125 mL of diethylene glycol (DEG), where a nominal concentration of Fe^{3+} and a molar ratio Fe to sodium acetate of 0.4 M and 3 are, respectively, chosen. Further details on the synthesis procedure were recently published elsewhere [15]. For the above quantities of chemicals, the calculated two main synthesis parameters including the hydrolysis ratio h (defined by the molar ratio: water/metal) and the acetate ratio τ_{Ac} (defined by the molar ratio: acetate ions/M^{2+}) were equal to ~7 and ~8, respectively. It is noteworthy that the as-produced NPs surface is expected to be covered with a certain amount of hydrophobic chemisorbed organic species, therefore for a Cr(VI) removal study purpose, a certain amount of each powder was calcined in air at 300°C for 24 h to remove these entities without altering the structure and the microstructure of the NPs.

2.2. Characterization techniques of the produced nanoparticles

The XRD patterns were measured by a PANalytical X-pert Pro powder diffractometer equipped with an X'Celerator detector and a cobalt anode. The XRD powder patterns analysis was carried out with a set of softwares [17]. Polycrystalline strain-free silicon was used as standard to quantify the instrumental broadening contribution and the average crystallite size and the strain were inferred from the diffraction peak broadening using the Williamson–Hall (W–H) method [18]. IR spectra were recorded on a on a Bruker Equinox FT-IR spectrometer over the range 400–4,000 cm^{-1} using the KBr pelleting technique (Bruker, Massachusetts, United States). The elemental metal atomic ratios were determined on a JEOL-100-CX II SEM microscope operating at 100 kV equipped with an EDX spectrometer (JEOL, Tokyo, Japan). The sample was placed onto conductive double-sided adhesive carbon-tabs tape supported aluminum stub and then dried with a secondary vacuum pump. Simultaneous TG/DTA of the as-prepared powders was recorded from ambient to 800°C in air with a heating rate of 10°C min^{-1} using a SETARAM TG-DTA-92 (SETARAM, Lyon, France). DC magnetic measurements on the low-temperature calcined powders were carried out with a SQUID PPMS VSM magnetometer. The hysteresis loops were measured at 300 K with a magnetic field cycling in the range ±50 kOe. The temperature dependence of the magnetization was recorded between 50 and 330 K under a constant magnetic field of 20 kOe. In this case, measurements were conducted under a zero-field cooling (ZFC) mode where the sample was cooled from room temperature in no applied field, then a magnetic field is applied while warming in the applied field.

2.3. Cr(VI) adsorption and NPs recycling experiments

Adsorption experiments were carried out at room temperature and at a fixed pH of ~2.0 using a batch technique. To adjust the pH, a 1.0 M HCl or a 1.0 M NaOH solution was used whenever needed. The mixing of the low-temperature calcined (at 300°C) produced NPs with Cr(VI) solutions (in the presence or in the absence of competitive ions) was performed in Pyrex glass test tubes with screw caps. For proper mixing and dispersion of the NPs in the Cr(VI) solutions, a power Sonic 240 ultrasound device was intermittently used with a vortexer. After mixing for a certain duration, the NPs were readily separated from the supernatant using a strong NdFeB magnet. For recycling experiments, the Cr(VI)–loaded NPs were dispersed in an excess of 0.5 M NaOH and the mixture was sonicated for about 5 min. The NPs were then collected by magnetic decantation, washed with ultrapure water until a colorless solution with a neutral pH is obtained. The obtained adsorbent was then dried in an oven and re-used in the succeeding Cr(VI) adsorption cycle.

2.4. Absorbance measurements

Absorbance of the Cr(VI) solutions was measured on a UV–visible double-beam Jasco V-670 spectrophotometer in the wavelength range 300–700 nm (Jasco, England). Further details on the experimental procedure were reported in a recent publication [15].

3. Results and discussion

3.1. Phase and structure

EDX spectra of the as-produced powders were recorded for all samples. Selected spectra are shown in Fig. 1. They showed the presence of the expected elements for instance, Fe, Co and Zn. Quantitative analysis of the EDX spectra (see the inset) leads to the determination of the chemical formulas as gathered in Table 1.

Except the sample with the nominal composition $x = 1.0$, as can be clearly seen from Table 1, the chemical composition of the remaining samples deviates from the expected nominal stoichiometry of the spinel-type ferrites, namely, $Co_xZn_{1-x}Fe_2O_4$ (x = 0.2, 0.4, 0.6, 1.0). Additionally, only the composition of Co element is close to its expected nominal content. The remaining two elements, Zn and Fe, showed lack and excess content, respectively, relative to their respective nominal compositions. Further, it is important to note the negligible Zn content compared with the other elements. Surely, the experimental synthesis conditions (refluxing temperature ~ 150°C, h ~ 7, τ_{Ac} ~ 8) favorite the Zn^{2+} dissolution in the DEG solvent forming soluble Zn^{2+} complexes with the dissolved species such as acetates and DEG derivatives instead of its entrance into the spinel-like structure. Therefore, we hereafter excluded Zn content from the experimental chemical formulas and we choose the approximate formulas given in Table 1 in which only the metallic elements Co and Fe are taken into consideration. Besides, to simplify the discussion, we denote the ferrite samples by their nominal Co compaction, (x = 0.2, 0.4, 0.6, 1.0), for instance, $x = 0.6$ for the experimental composition, $Co_{0.56}Fe_{2.26}O_4$. The XRD patterns of the three as-produced powders are illustrated in Fig. 2.

For all samples, XRD analysis reveals the formation of single phase without any additional foreign phase such as magnetite, maghemite or any other metal oxide. The diffraction peaks can be indexed in the cubic spinel-type structure (S.G. No. 227, Fd-3m). The refined unit cell parameters of the produced ferrites range from 8.385(1) (x ~ 0.2) to 8.407(2) Å (x

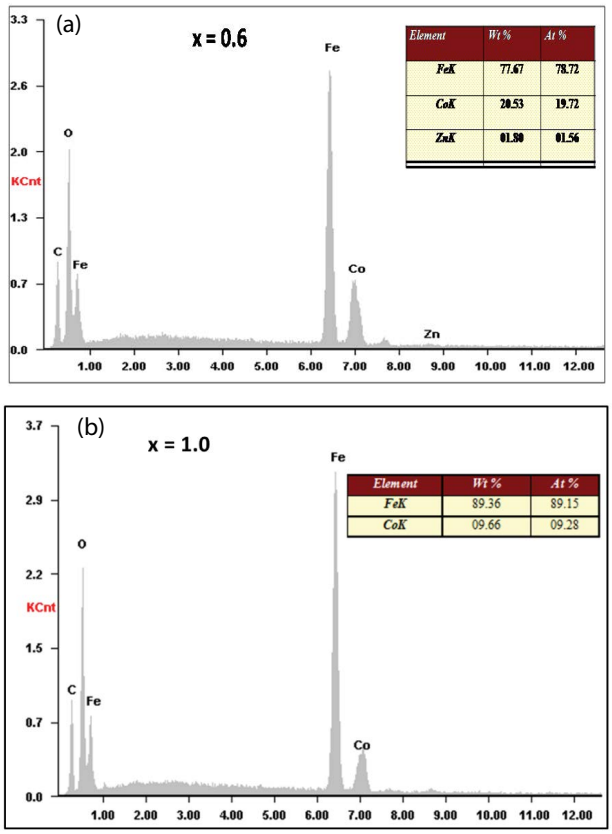

Fig. 1. Selected EDX spectra (x ~ 0.6, 1.0) of the as-produced powders with the chemical formula $Co_x^{2+}Fe_{\frac{8-2x}{3}}^{3+}O_4$ (x ~ 0.2, 0.4, 0.6, 1.0). The EDX peak with the lowest energy is due to carbon arising from both the sample holder and a small amount of organic entities grafted on particles surface.

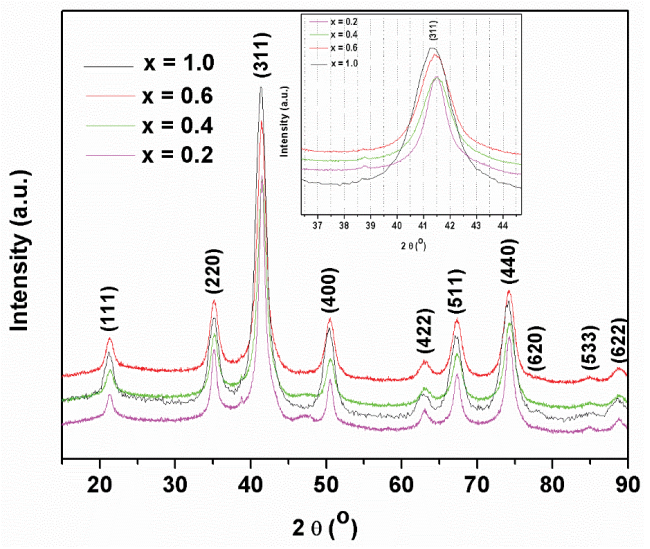

Fig. 2. Indexed XRD patterns of the as–prepared powders. The inset is a zoom-view around the (311) peak showing the relative shift of XRD peaks.

~ 1.0). These values are in the normal range of transition metal spinel ferrites [17,19,20]. Additionally, the general trend in lattice parameter change is an increase with the Co composition, x, increase, in consistency with the difference in the ionic radius between Co^{2+} and Fe^{3+} cations [21]. FTIR analysis was performed in order to confirm the spinel structure of the produced ferrites and to characterize their surface chemistry. Fig. 3 shows that the IR spectra of the as-produced ferrites.

The spectra can be viewed as divided into three regions: (i) A low-frequency region (~400–700 cm^{-1}) which exhibited the spinel-type ferrite features [22]; two bands located at ~565 to 597 and 428 cm^{-1} were clearly observed. They are associated to the vibration of oxide ions against the cations located in the tetrahedral (A) and in the octahedral (B) sites, respectively. (ii) A medium frequency region (~1,000–1,600 cm^{-1}) showing the features of the polyol and acetate species grafted onto the surface of NPs; for instance, the two bands located at ~1,400 and 1,600 cm^{-1} are assigned to the symmetric and asymmetric vibrations of acetate ions, respectively, whereas, the other two bands in the range 1,050–1,150 cm^{-1} are due to the C–O–C/C–O elongations. These assignments are supported by the presence of very weak couple of sharp bands located at 2,920/2,880 cm^{-1} (see the inset) associated with asymmetric/symmetric C–H vibrations. (iii) The high frequency region (over 3,000 cm^{-1}) shows an intense broad band centered at ~3,350 cm^{-1} associated with the O–H stretching of water molecules and the hydroxyl ions (OH^-) of the alkaline reaction medium. Thermal behavior of the as-produced powders was studied by XRD and TG/DTA. The TG/DTA curves of the as-prepared powders are presented in Fig. 4. It appears a slight initial endothermic signal associated to a mass loss up to 150°C due to the removal of adsorbed water. Then, a strong exothermic effect appears with a maximum at around

Table 1
Experimental chemical formula, approximate chemical formula and selected structural and microstructural characteristics inferred from EDX, XRD and IR of the as-produced powders with the chemical formula $Co_x^{2+}Fe_{\frac{8-2x}{3}}^{3+}O_4$ (x ~ 0.2, 0.4, 0.6, 1.0)

	Experimental chemical formula	Approximate chemical formula	a/Å	L_{XRD}/nm	$<D_{TEM}>$/nm	ε_{XRD} (×10²)	$\nu_{(Fe...O)}$/cm^{-1}	
0.2	$Co_{0.23}Zn_{0.07}Fe_{2.47}O_4$	$Co_{0.2}Fe_{2.47}O_4$	8.385(1)	7.7	7.0 ± 1.2	0.013	565	428
0.4	$Co_{0.36}Zn_{0.05}Fe_{2.39}O_4$	$Co_{0.4}Fe_{2.39}O_4$	8.385(2)	6.9	6.6 ± 1.0	5.0	577	428
0.6	$Co_{0.56}Zn_{0.04}Fe_{2.26}O_4$	$Co_{0.6}Fe_{2.26}O_4$	8.397(3)	5.9	5.2 ± 1.1	3.0	577	428
1.0	$Co_{0.97}Fe_{2.02}O_4$	$CoFe_2O_4$	8.407(2)	5.4	4.6 ± 0.9	0.015	597	–

240°C–260°C accompanied with an important mass loss in the ~150°C–500°C range. The thermal effect is attributed to the combustion of the organic entities (polyol and acetate) grafted on the surface of the NPs.

The organic species are likely chemisorbed on the NPs surface since their complete removal takes place at relatively high temperatures. The interpretations are supported by the complete disappearance of the IR features of the mentioned chemical species, namely the organic and hydroxyl groups from the IR spectra (not shown) of samples calcined at 500°C. As can be seen, beyond ~550°C, the DTA curves show an additional exothermic peak without any noticeable mass variation. In order to find an explanation for the last exothermic peak, XRD patterns of as-produced powders annealed at 1,000°C for 4 h were recorded (Fig. 5). All XRD patterns revealed a mixture of two phases consisting a spinel-type ferrite (PDF No. 22–1086) and the hematite (α–Fe_2O_3: PDF No. 33-0664). The fraction of α–Fe_2O_3 is very low in the case of the composition $Co_{0.97}Fe_{2.02}O_4$ (x = 1.0).

Three possible explanations can be derived for the interpretation of the thermal behavior of the as-produced ferrites beyond ~550°C, (i) the as-prepared powders could be a mixture of a stoichiometric ferrite and maghemite (γ–Fe_2O_3). Indeed, it has been reported that maghemite readily transforms into hematite with a size-dependent transition temperature; The larger the NPs size, the higher the transition temperature [23]. (ii) The as-produced powders consist of a mixture of a stoichiometric ferrite ($M^{(II)}Fe_2^{(III)}O_4$) and magnetite (Fe_3O_4). Upon heating in air, the later readily oxidizes into hematite [21], (iii) the as-produced powders could be

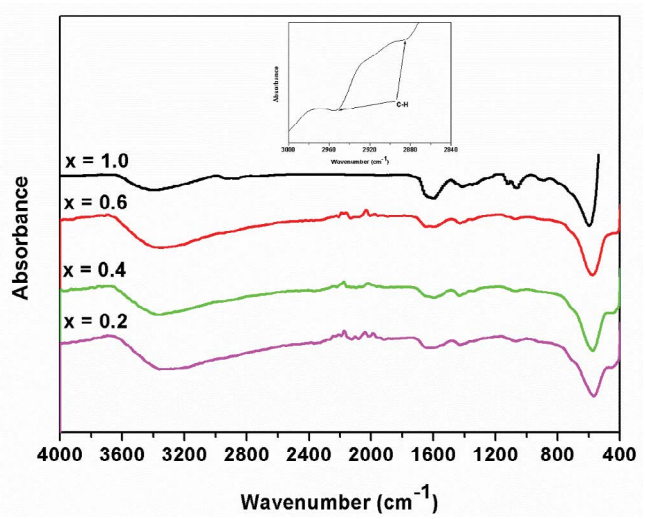

Fig. 3. IR spectra of the as-prepared cobalt ferrites.

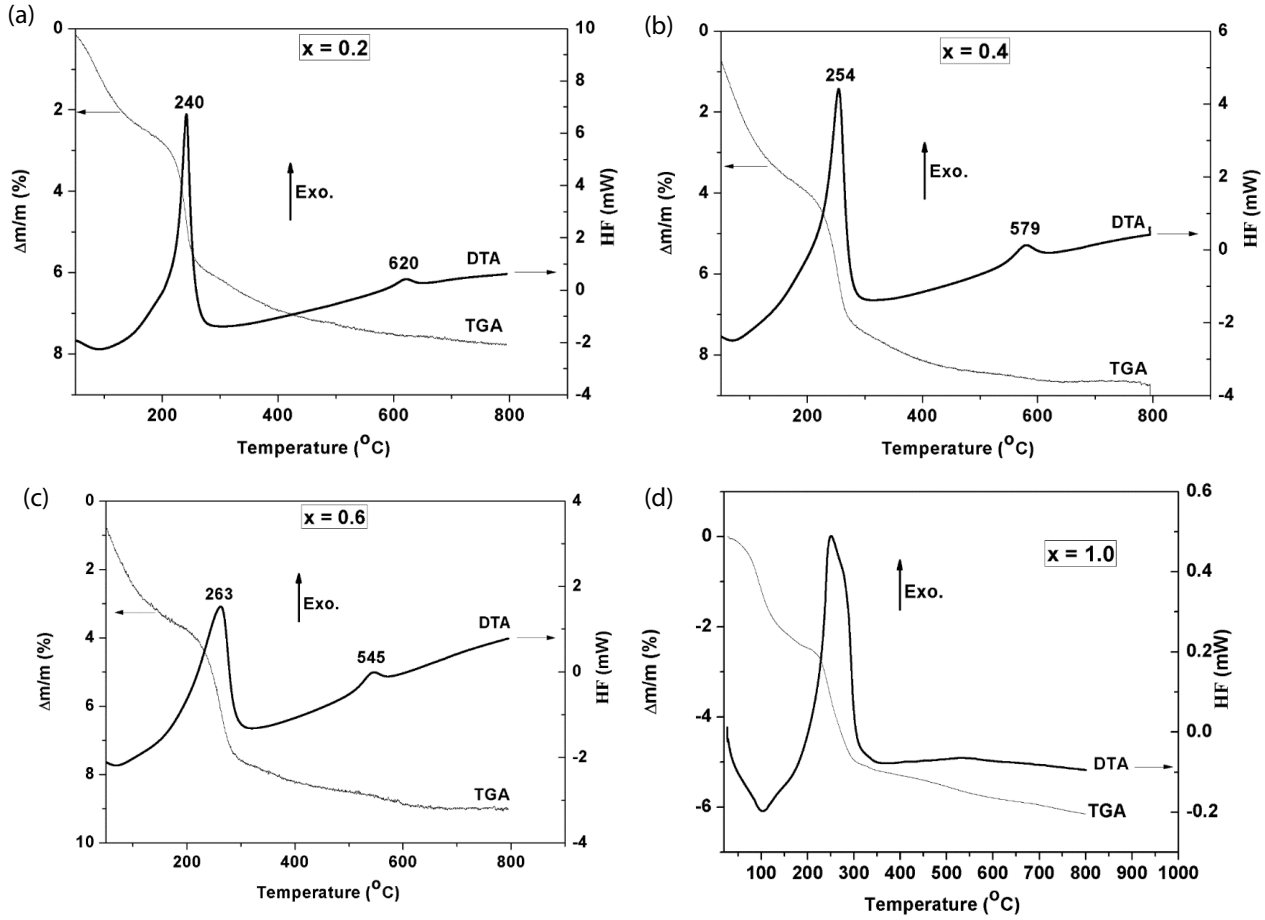

Fig. 4. TG/DTA thermograms of the as-prepared cobalt ferrites (x ~ 0.2 (a), 0.4 (b), 0.6 (c), 1.0 (d)).

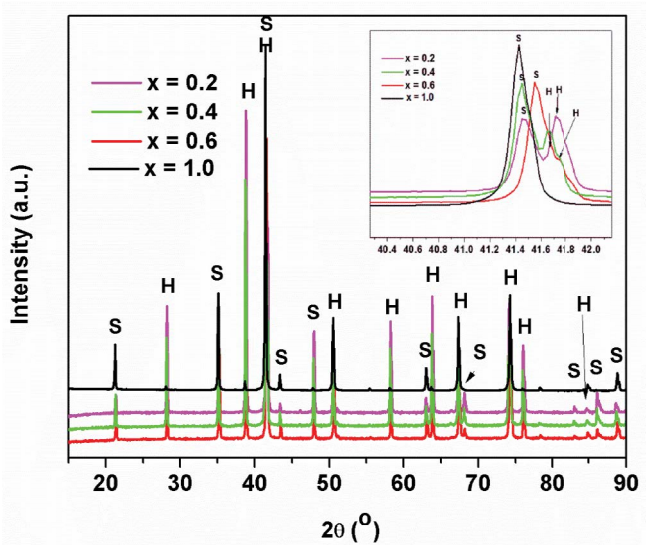

Fig. 5. XRD patterns of the as-prepared powders calcined at 1,000°C for 4 h. The inset is a zoom-view comparing the relative intensity of the characteristic peak of hematite phase. The symbols *S* and *H* refer to peaks belonging to the structure of spinel and hematite, respectively.

single phases of a non-stoichiometric cobalt ferrites. The ferrite can be viewed as a solid solution of a stoichiometric ferrite and maghemite with vacancies in the *octahedral* sites [24]. The first hypothesis (i) can be ruled out, since the few additional XRD peaks characterizing γ-Fe_2O_3 at low angles (PDF No. 39-1346) could not be observed for the as-prepared powders, despite the important amount of hematite yielded upon calcination, especially for $x \neq 0$. The second hypothesis (ii) can be also discarded since no traces of Fe^{2+} were detected by chemical titration (results not provided). Besides, regarding the synthesis conditions, the reaction medium acts as a highly oxidizing agent [23]. Therefore, formation of Fe_3O_4 by partial reduction of Fe^{3+} to Fe^{2+} is excluded.

Considering the remaining proposition (iii), the chemical formula of our as-produced samples can be assumed as non-stoichiometric ferrites with the following chemical formula:

$$Co_x^{2+}Fe_{\frac{8-2x}{3}}^{3+}V_{\frac{1-x}{3}}O_4 \quad (1)$$

where V denotes a cation vacancy and x the chemical composition of Co^{2+} as determined by EDX. From Eq. (1), we can notice that deviation from the stoichiometry can be measured by the coefficient x; stoichiometric ferrite corresponds to $x = 1$, while a non-stoichiometric one (with excess of Fe^{3+} and lack of Co^{2+}) corresponds to $x < 1$.

Based on XRD results, we propose the following decompositional reaction scheme:

$$Co_x^{2+}Fe_{\frac{8-2x}{3}}^{3+}V_{\frac{1-x}{3}}O_4 \rightarrow \frac{4}{3}(1-x)Fe_2O_3 + xCoFe_2O_4 \quad (2)$$

From Eq. (2), we can notice that the larger the coefficient, x, the larger the Co^{2+} content, the lower the Fe^{3+} content and the amount of hematite formed and vice versa. Therefore, relative mass of α-Fe_2O_3 should increase with the decrease of x from ~1.0 (which corresponds to $Co_{0.56}Fe_{2.26}O_4$) to ~0.2 (which corresponds to $Co_{0.23}Fe_{2.47}O_4$). The interpretation is in concordance with the XRD results. Indeed, as can be clearly seen from the inset of Fig. 5, the relative intensity of α-Fe_2O_3 increased in monotonous manner with the x decrease, thus indicating the relative increase of the amount of hematite to that of spinel-type ferrite phase with the x decrease. Additionally, the Bragg positions of XRD peaks of the spinel phase are in excellent agreement with those of the cobalt ferrite, $CoFe_2O_4$ (PDF No. 22-1086) thus supporting the decompositional scheme (2). So, the exothermic peak observed in the DTA curves of the as-produced ferrites beyond ~550°C (Fig. 4) is very likely to be associated with the thermal decomposition of our ferrite samples according to Eq. (2).

3.2. Microstructure

W–H analysis was performed for all the as-produced samples. A typical W–H plot is displayed in Fig. 6.

The average crystalline size (L_{XRD}) and the lattice strain (ε_{XRD}) are depicted in Table 1. The mean crystallite size values range from ~5 to ~8 nm indicating the formation of ultrasmall crystallites. Besides, ε values of all the as-prepared are very small, thus demonstrating high quality crystallites in terms of crystallinity. TEM images were performed for all the as-produced samples. Selected TEM images (x ~ 0.6 and ~1.0) with associated particle size distribution histograms are shown in Fig. 7.

TEM analysis evidences the formation of roughly spherical NPs. The average diameter with the standard deviation of the nanograins, obtained by measurements of at least 150 particles from random TEM images is given in Table 1. It can be noticed that the average particle diameter for all samples is consistent with the average size of the crystallites calculated from XRD data indicating that the nanograins are single crystals.

3.3. Magnetism

The temperature dependence of the magnetization, M vs. T under a ZFC mode is presented in Fig. 8.

The ZFC plots show a broad maximum at a critical temperature called the blocking temperature, T_b, above which magnetic NPs behave as superparamagnets. T_b represents the average threshold temperature above which magnetic anisotropy barrier is overcome by thermal activation energy solely, causing NPs to relax from a blocked state (ferrimagnetic) to the superparamagnetic state. For all samples, T_b, is below room temperature (Table 2) suggesting a superparamagnetic behavior of the NPs at room temperature. It ranges between 130 K (x ~ 0.2) and 187 K (x ~ 1.0).

The blocking temperature features (average value and distribution) depends on at least four fundamental interdependent parameters: the chemical composition, the particle size, the particle shape, the particle size distribution and the strength of inter-particle magnetic interaction [25–27]. In our case, at least three parameters are varying simultaneously (the chemical composition, the particle

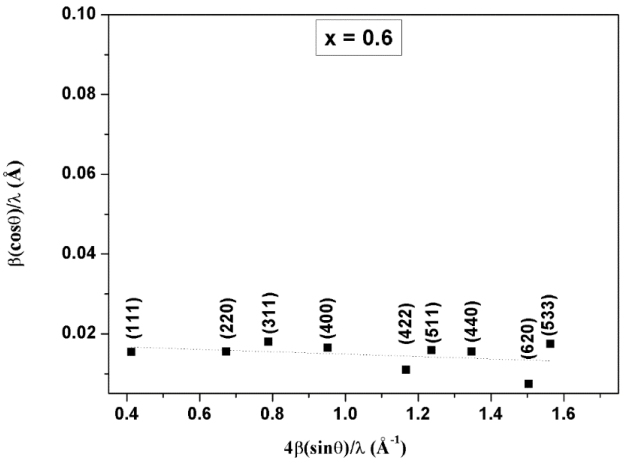

Fig. 6. A typical W–H plot for the as-prepared cobalt ferrite (x ~ 0.6). The straight line is the best fit to the data points.

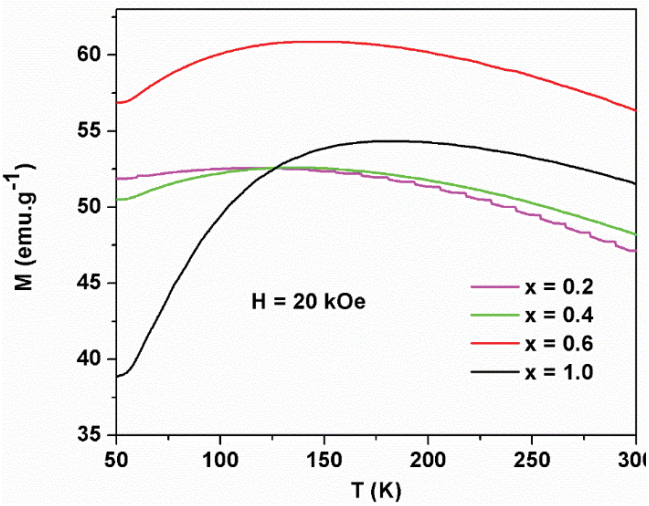

Fig. 8. ZFC thermal variation of the magnetization measured under a magnetic field of 20 kOe for the low-temperature calcined ferrites.

size and the strength of inter-particle magnetic interaction). These parameters could compete in opposite manner which makes impossible the interpretation of the variation of average T_b from one sample to another. The large broadness of ZFC curves around T_b indicates large distribution of blocking temperature due to large particle size distribution. The larger T_b values being attributed to biggest NPs [26]. Note, magnetic measurement under a field cooling (FC) mode (not performed) could permit a clear distribution of the T_b through the examination of divergence between the FC and ZFC curves [27]. For nanostructured ferrites, at temperatures above the blocking temperature, T_b, and below the Curie temperature, T_C, M vs. T is often described by a modified Bloch's law function [28]:

$$M(T) = M(0)\left[1 - \left(\frac{T}{T_C}\right)^{\beta}\right] \tag{3}$$

where M (0) is the spontaneous magnetization at 0 K, T_C is the Curie temperature, and β is the so-called Bloch's exponent.

The magnetization as a function of temperatures above the blocking temperature, T_b, is plotted in Fig. 9.

A good fitting of our data to the modified Bloch's law is obtained. The modified Bloch's law parameters are gathered in Table 2. The Bloch's exponent ranges between 2.2 and 3.2. It is remarkably larger than that of the Bloch's exponent value (3/2) calculated for an infinitely large ferrite system. For a give chemical composition, as compared with a bulk material counterpart, the deviation from the normal ($T^{3/2}$) observed for our nanoferrites corresponds to a change in the the magnetic structure (via the occupancy change of the metal ions over the tetrahedral [A] and the octahedral [B] sites of the spinel-type structure), and/or the microstructure (size and shape) and/or the surface chemistry of the material [29]. In our case, the interpretation of β values and its variation from one cobalt ferrite to another is hard since we believe that there should be a remarkable difference between the low-temperature calcined four ferrites of at least three factors, namely the chemical composition,

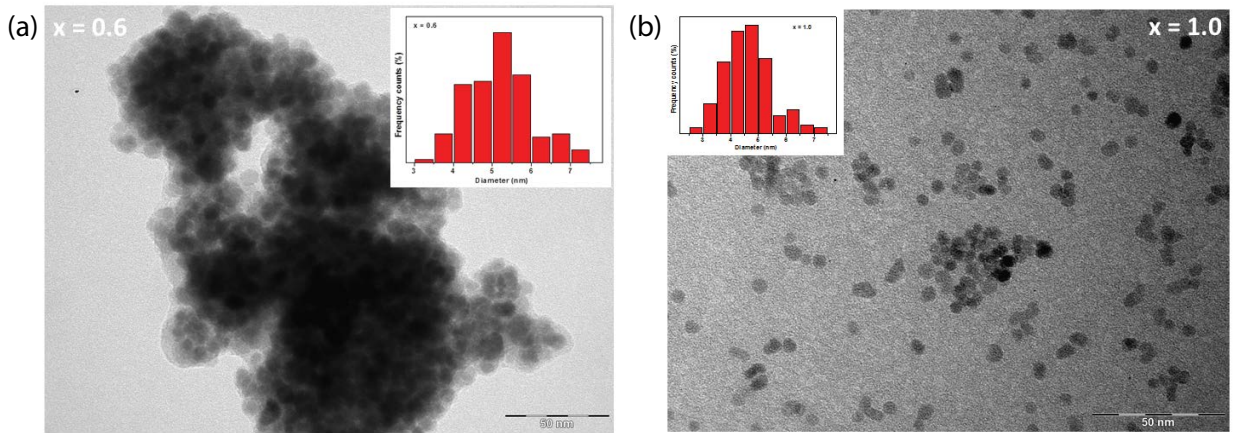

Fig. 7. Typical TEM images of the two as-prepared powders (x ~ 0.6, x ~ 1.0) with their corresponding particle size distribution histograms (the inset).

Table 2
Main magnetic characteristics of the low-temperature calcined non-stoichiometric cobalt ferrites (x ~ 0.2, 0.4, 0.6, 1.0)

x	T_b/K	M_{sat} (300 K)/emu g^{-1}	H_c (300 K)/Oe	M_{Rem} (300 K)/emu g^{-1}	M (0)/emu g^{-1}	T_C/K	β	$T_{1/2}$/K
0.2	130	57	394	10.0	54.6	745	2.2	541
0.4	132	58	196	5.5	53.6	704	2.7	547
0.6	158	69	219	6.0	61.9	697	2.9	546
1.0	187	81	360	7.5	55.5	672	3.2	552

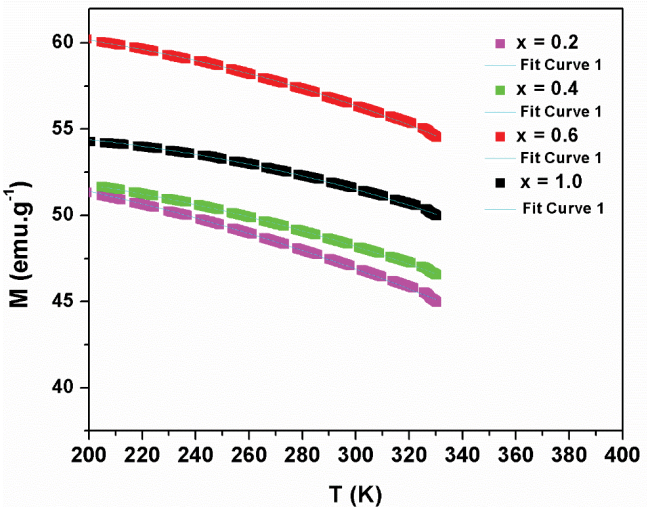

Fig. 9. A portion of ZFC thermal variation (at high temperatures) of the magnetization measured under a magnetic field of 20 kOe for the low-temperature calcined ferrites. The continued fine line associated with each M vs. T curve represents the best fit of the data points to the Bloch's law equation.

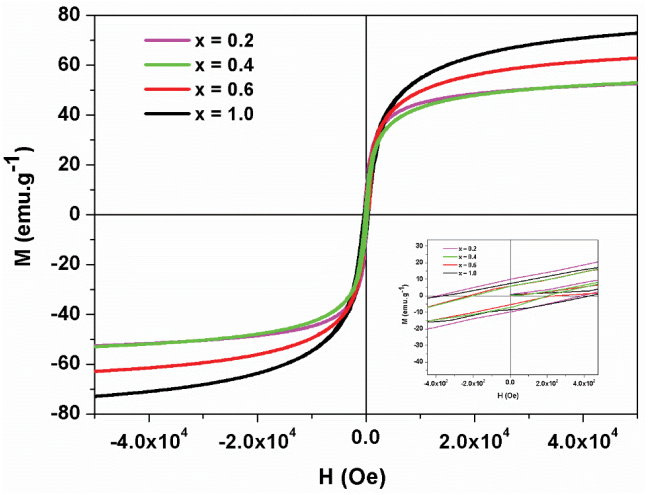

Fig. 10. Hysteresis loops measured at 300 K for the low-temperature calcined ferrites.

the magnetic structure and the size of NPs. The calculated Curie temperature, T_C, ranges between 672 and 745 K for x ~ 1.0 and x ~ 0.2, respectively. These values are comparable with those reported for cobalt nanoferrites having comparable chemical composition [20], but they are notably lower than the value (793 K) reported for the bulk $CoFe_2O_4$ [19]. Here again, the noticeable difference between the T_C values of our materials should be mainly due to the difference the chemical composition, the crystal structure and the size of NPs. Additionally, as can be noticed from Fig. 9, the magnetization decay is low; For example, the temperature values ($T_{1/2}$) at which the magnetization is reduced to the half is above 540 K (Table 2). For a practical purpose, the temperature, $T_{1/2}$, is of importance since the produced materials could be integrated in systems that work in high temperature conditions while maintaining reasonable magnetization.

Magnetization (M) vs. applied field (H) curves recorded at 300 K for the low-temperature calcined NPs are presented in Fig. 10.

As expected, $M(H)$ curves did not evidence any hysteresis feature, in agreement with the superparamagnetic behavior of the particles above the blocking temperature. In addition, as expected for ferrimagnetic materials, the magnetization, M, increases rapidly with magnetic field increase, then gradually tends to saturation at high applied magnetic fields. The saturation magnetization, M_{sat}, was determined by extrapolating M vs. $1/H$ curve to $1/H = 0$. As can be noticed from Table 2, the saturation magnetization follows a trend similar to the blocking temperature, T_b. It ranges between 57 for the ferrite with x ~ 0.2 to 81 emu g^{-1} for the ferrite with x ~ 1.0. In spinel-type ferrites, the M_{sat} value is strongly sensitive to several parameters including the chemical composition, the cation distribution over the spinel sites, namely, A and B sites and the average particle size [30,31]. Due to the complex interplay between the parameters and their strong dependence on the physico-chemical conditions of the synthesis, a clear interpretation of the difference between the M_{sat} values of the four ferrites is impossible. A zoom view of the $M(H)$ curves at low applied fields (see the inset in Fig. 10) shows a weak hysterics loops (non-zero coercive field and non-zero remanence) for all samples suggests the existence of a small fraction large sized of NPs exhibiting a blocking temperature, T_b, above 300 K.

3.4. Cr(VI) removal study

Batch experiments for the removal of Cr(VI) species from Cr(VI)-contaminated synthetic aqueous solutions using the different low-temperature calcined NPs, namely the nanoferrites with the Co compositions x ~ 1.0, 0.2, 0.4 and 0.6, was carried out at room temperature at an initial pH of 2.0. The effect of various factors such as, the NPs dose, the initial Cr(VI) ions concentration, the contact time and

the coexisted ions, which could influence the adsorption process was investigated.

3.4.1. Effect of NPs dose

The effect of adsorbent dose was carried out on 10 mL 50 mg L^{-1} Cr(VI) solution treated by NPs with doses varying between 0.5 and 7.0 g L^{-1} under a contact duration 10 min. and a pH of ~2.0. Similar UV–visible absorbance spectra were recorded for all the four compositions. Fig. 11 shows the UV–visible spectra of the treated solutions along with the untreated one of a selected cobalt composition (x ~ 0.4) and the inset shows photos taken on selected doses indicating the evolution of the supernatant color with the increase of the NPs dose.

The intensity of the characteristic absorbance band of the Cr(VI) species decreased drastically with the increase in NPs dosage due to the important decrease in Cr(VI) concentration. The observation is confirmed by the yellowish color change of the supernatant (see the inset) which fades gradually with the increase of the NPs dose. Fig. 12 shows the removal percentage variation of Cr(VI) species on the NPs surface as a function of NPs dose for all compositions.

As expected, the removal percentage increases in a monotonous manner with the increase of NPs dose to reach a maximum removal of 100% for a NPs dose of about 7.0 g L^{-1}. For a given Cr(VI) concentration, as the amount of the adsorbent increased, the specific NPs surface increased and consequently the active sites for the adsorption of Cr(VI) increased until the complete removal of the entire amount of the initially introduced Cr(VI) species. Additionally, for a given NPs dose less than 7.0 g L^{-1}, the better removal % was observed with the samples with the compositions x ~ 1.0 and ~0.6. While the minimum removal % was observed with the sample x = 0.2. The trend in the removal % could be interpreted on the basis on the variation of the mean NPs size; the NPs of the compositions x ~ 1.0 and ~ 0.6 have the smallest size (Table 1) and the higher removal %. While, the sample with x ~ 0.2 have the larger NPs size and the lower removal %. Hereafter, we focus our study on the compositions x ~ 1.0 and ~0.6 rather than all the compositions.

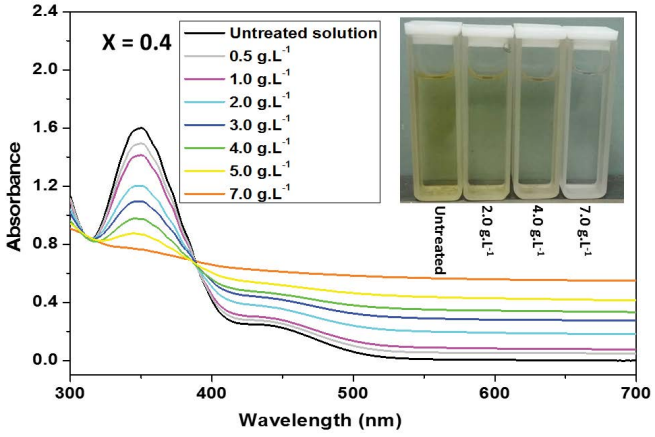

Fig. 11. Typical absorbance spectra of 10 mL 50 mg L^{-1} Cr(VI) solution treated by different doses of the low-temperature calcined ferrite with x ~ 0.4. The inset compares selected photos of the treated solutions with the untreated one.

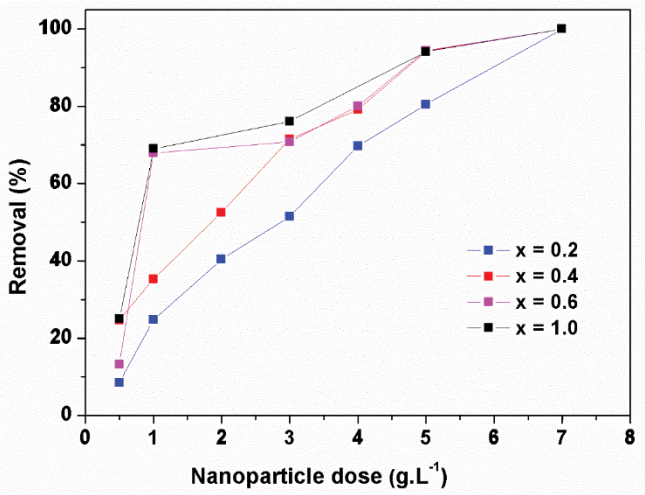

Fig. 12. Cr(VI) removal percentage from 10 mL 50 mg L^{-1} Cr(VI) solution treated by various doses of the calcined cobalt ferrites (x ~ 0.2, 0.4, 0.6, 1.0).

3.4.2. Effect of initial Cr(VI) concentration and contact time

The kinetics of Cr(VI) removal on the NPs of the samples x ~ 1.0 and ~0.6 was conducted on solutions at various initial Cr(VI) concentrations ranging from 30 to 100 mg L^{-1} in the presence of 4.0 g L^{-1} of adsorbent. UV–visible spectra (not shown) were measured for different contact times in the range 1–50 min. From the spectra, it is possible to calculate the removal percentage of Cr(VI) for any time t by applying the following equation:

$$\text{Removal}(\%) = \frac{C_i - C_t}{C_t} \times 100 \quad (4)$$

where C_i and C_t are the initial concentration (mg L^{-1}) of Cr(VI) and the concentration of these species after any contact time t (min) with the NPs, respectively. Removal % vs. the contact time, t, for different Cr(VI) compositions are presented in Fig. 13.

The rate of Cr(VI) uptake takes place in two phases. An initial phase involving rapid metal species uptake followed by a subsequent much slower removal rate which gradually reach an equilibrium state. For all concentrations more than 80% of the removable Cr(VI) took place during the first 10 min. The rapid adsorption of Cr(VI) by the NPs is attributed to the external surface adsorption, which is different from the other adsorbing mechanism such as the microporous adsorption process. Since an important fraction of the adsorption sites of the NPs exist in the exterior of the adsorbent compared with the porous adsorbent, it is easy for the adsorbate to access these active sites, thus resulting in a rapid approach to equilibrium. Additionally, it is clearly seen that the equilibrium time is a concentration–dependent parameter. It is very short for

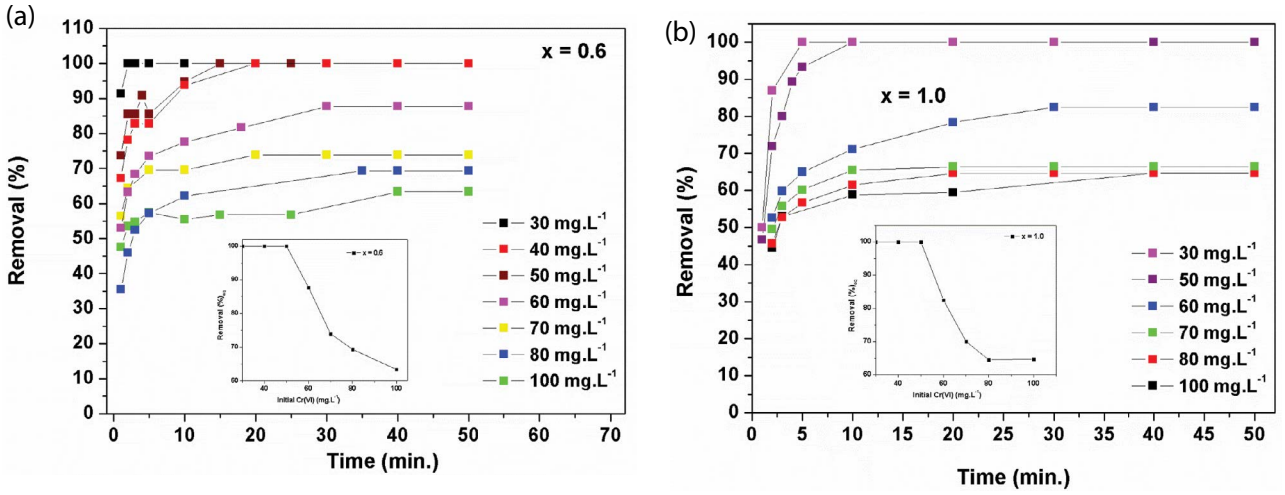

Fig. 13. Cr(VI) removal efficiency by 4 g L^{-1} NPs of the low-temperature calcined cobalt ferrites ((a) x ~ 0.6 and (b) x ~ 1.0) as a function of contact time for different initial Cr(VI) concentrations. The inset depicts the removal percentage vs. the initial Cr(VI) concentration at equilibrium state.

the low initial Cr(VI) concentration and increased gradually with the increase of concentration. Further, the similar shape of the curves at each initial concentration indicated that the percentage adsorption of Cr(VI) decreased with the increase of the initial Cr(VI) concentration. This is expected since for a fixed adsorbent dosage, the total available adsorption sites are limited thus leading to a decrease in percentage removal of the adsorbate. At equilibrium, the removal efficiency of Cr(VI) was found to be vary between ~65% and 100% for the concentrations ranging from 30 to 100 mg L^{-1} (see the inset of Fig. 13).

Three adsorption kinetic models including the pseudo-first-order model, the pseudo-second-order model and intraparticle diffusion model were tested to determine the more probable adsorption mechanism of the Cr(VI) species onto the selected two ferrites NPs at pH 2.0. The integrated forms of the three models are, respectively, expressed as [32]:

$$\ln\left(q_e - q_t\right) = \ln\left(q_e\right) - k_1 t \tag{5}$$

$$\frac{t}{q_t} = \frac{1}{k_2 \times q_e^2} + \frac{t}{q_e} \tag{6}$$

$$q_t = k_3 \times t^{1/2} \tag{7}$$

where q_t (in mg g^{-1}) is the adsorption capacity of the NPs at any time t (in min), q_e (in mg g^{-1}) is the adsorption capacity at equilibrium time, k_1 (in min^{-1}) is the rate constant for the pseudo-first-order adsorption process, k_2 (g mg^{-1} min^{-1}) is the rate constant for the pseudo-second-order adsorption, k_3 (mg g^{-1} $min^{-1/2}$) is the intraparticle diffusion rate constant and C is the intercept.

The adsorption capacity q_t, (in mg g^{-1}) at any time t (including the equilibrium time) is calculated from the following relation:

$$q_t = \frac{C_i - C_t}{m} \times V \tag{8}$$

where C_i and C_t (in mg L^{-1}) are the initial concentration of Cr(VI) and the concentration of these species after a contact, t (in min), with the ferrite NPs, respectively and V (in L) is the volume of the supernatant (assumed to be that of the initial volume of the Cr(VI) solution used for each removal essay) and m is the mass of sorbent used (in g).

Plots of the experimental data of selected compositions, according to the above-mentioned models are shown in Fig. 14.

It can be seen that for the experimental data plotted on the basis of Eqs. (5) and (7) associated to the pseudo-first-order model (Fig. 14a) and the intraparticle diffusion model (Fig. 14c), respectively, clearly depart from the linearity. On the other hand, the experimental data plotted according to Eq. (6) associated to the pseudo-second-order (Fig. 14b) show a good linearity with a correlation coefficient better than 0.998 for both compositions x ~ 0.6 and ~1.0. Parameters of pseudo-second-order for Cr(VI) adsorption onto the ferrite NPs $Co_x^{2+}Fe_{\frac{8-2x}{3}}^{3+}O_4$ (x ~ 0.6, 1.0) for selected Cr(VI) initial concentrations along with the corresponding correlation coefficients (R^2) are summarized in Table 3.

The results indicated that the pseudo-second-order sorption mechanism is predominant for the sorption of the hexachromium entities onto our nanoferrites, and it is considered that the rate of the sorption process is controlled by the chemisorption process. The mechanism involves valence forces through sharing or exchange of electrons between sorbent and sorbate as covalent forces [33]. From Table 3, it can be noted that the adsorption capacity, q_t, become noticeably larger for high adsorbate concentration. For instance, in the targeted Cr(VI) initial concentrations, the calculated maximum adsorption capacity at equilibrium was found for the concentrations 100 mg L^{-1}. It is of ~14.5 and ~16.5 mg L^{-1} for x ~ 0.6 and ~ 1.0, respectively. This can be explained by the fact that more targets of Cr(VI) provide higher driving force to facilitate the ion diffusion from the solution to the positively charged NPs surfaces, and therefore more collisions between Cr(VI) ions and active sites of the sorbent.

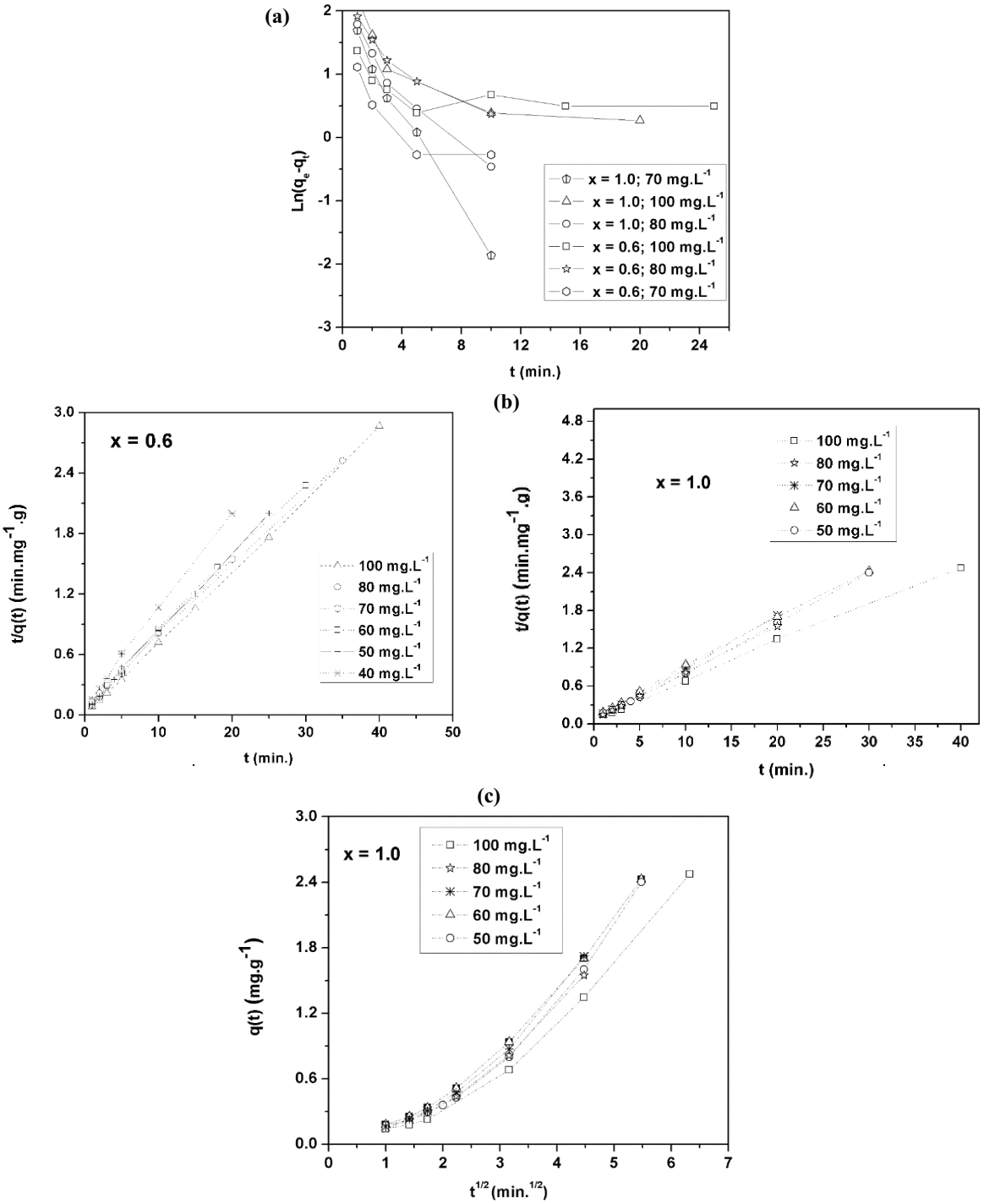

Fig. 14. Selected plots of the experimental data points (with dotted lines as a guide to the eye) according to the equations associated to the pseudo-first-order (a), the pseudo-second-order (b) and the intraparticle diffusion (c) models of the sorption kinetics of Cr(VI) species onto the studied nanoferrites (x ~ 0.6, x ~ 1.0) at various initial Cr(VI) concentrations.

3.4.3. Adsorption isotherms

To determine the adsorption capacity of the NPs, the equilibrium data for the adsorption of Cr(VI) onto 4 g L^{-1} NPs are analyzed in the light of the Langmuir and Freundlich adsorption isotherm models [34,35]. The Langmuir isotherm model predicts the existence of monolayer coverage of the sorbate molecules over a homogeneous sorbent surface without any interaction between the adsorbed species. The Langmuir model also assumes that the sorbent surface contains only one type of binding site so the energy of sorption is constant. Whereas, the Freundlich isotherm model assumes

Table 3
Parameters of pseudo-second-order for Cr(VI) adsorption onto the ferrite NPs $Co_x^{2+}Fe_{\frac{8-2x}{3}}^{3+}O_4$ (x ~ 0.6, 1.0) for selected Cr(VI) initial concentrations

C_i (mg L^{-1})	50		60		70		80		100	
x	0.6	1.0	0.6	1.0	0.6	1.0	0.6	1.0	0.6	1.0
R^2	0.999	0.999	0.999	0.998	0.999	0.999	0.999	0.999	0.999	0.998
Cr(VI) removal (%)	100	100	87.8	82.5	73.9	70	69.4	64.5	63.3	64.7
$q_{e,exp.}$ (mg g^{-1})	12.5	12.5	13.16	12.37	12.93	11.61	13.87	12.91	15.83	14.87
$q_{e,calc.}$ (mg g^{-1})	12.82	12.98	13.33	12.82	13.15	12.13	14.06	13.50	14.49	16.48
K_2 (mg g^{-1} min^{-1})	0.137	0.100	0.073	0.052	0.185	0.104	0.058	0.079	0.063	0.050

a heterogeneous sorption surface with sites that have different energies of sorption and provides no information on the monolayer adsorption capacity. The Langmuir and Freundlich isotherm models can be, respectively, presented by the following linear equations:

$$\frac{C_e}{q_e} = \frac{C_e}{q_{\max}} + \frac{1}{b \times q_{\max}} \tag{9}$$

$$\ln(q_e) = \ln(k_f) + \frac{1}{n}\ln(C_e) \tag{10}$$

where C_e and q_e are the concentrations of Cr(VI) (mg L^{-1}) in the solution and the adsorption amount per unit mass of NPs (mg g^{-1}) at the equilibrium state, respectively, $q_{\max}$ (mg g^{-1}) is the Langmuir constant related to the maximum monolayer sorption capacity and b (L mg^{-1}) is the constant related to the free energy or net enthalpy of adsorption, k_f is a constant related to sorption capacity (mg g^{-1}) and $1/n$ is an empirical parameter related to sorption intensity. The values of the above cited parameters are determined from the plot of C_e/q_e vs C_e and log(q_e) vs log (C_e) plots. The value of n varies with the heterogeneity of sorbent and gives an idea for the favorability of sorption process. It should be less than 10 and higher than unity for favorable sorption conditions. The experimental data were treated by the Langmuir and Freundlich models (Fig. 15).

It can be seen that the experimental data of Cr(VI) on the NPs fitted well into Langmuir isotherm model (Fig. 15a) with a correlation coefficient better than 0.97. Values of (q_{max}, b) calculated from the fitting results are of (13.3 mg g^{-1}, 0.6) and (17.0 mg g^{-1}; 0.3) for x ~ 1.0 and ~0.6, respectively. For the Langmuir model, it is estimated by a dimensionless separation factor whether the sorption is favorable or not. The separation factor, R_L, is defined as:

$$R_L = \frac{1}{1 + bC_i} \tag{11}$$

where C_i (mg L^{-1}) is the initial concentration of Cr(VI), b (L mg^{-1}) is the Langmuir constant. Values of $0 < R_L < 1$ indicates that the sorption is favorable. In the present study, R_L lies in the range of 0.015 and 0.029 for x ~ 1.0 and in the range of 0.036 and 0.068 for x ~= 0.6 revealing the feasibility of the adsorption process.

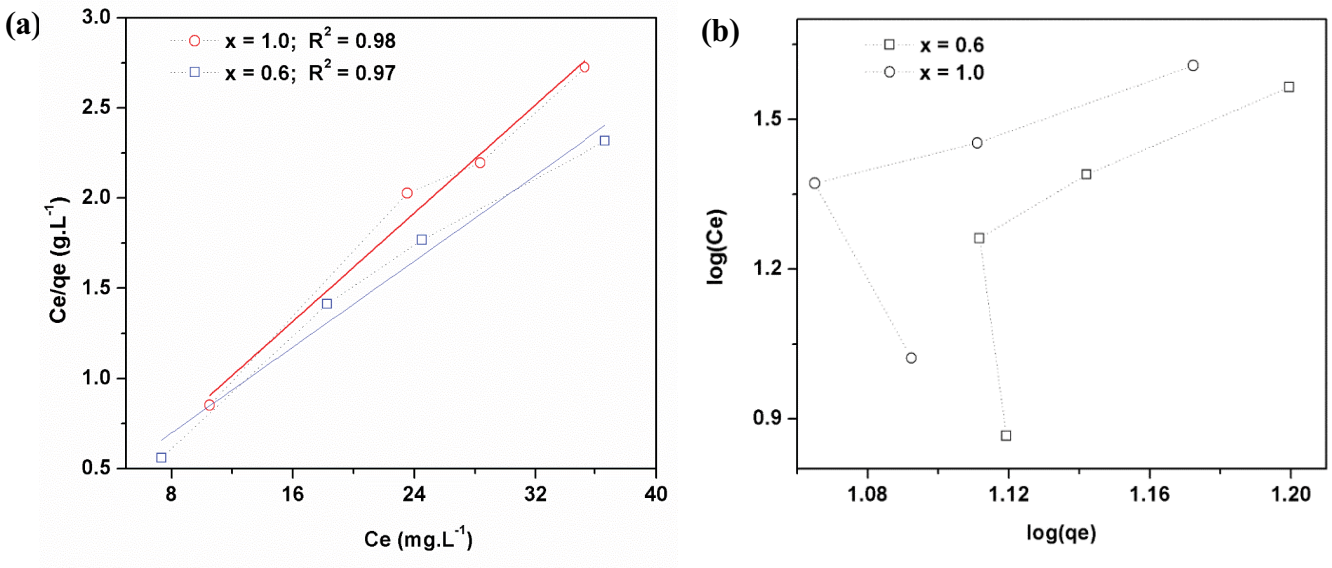

Fig. 15. Selected plots of the experimental data points (with dotted lines as a guide to the eye) according to the equations associated to the Langmuir (a) and Freundlich (b) models. The colored solid in (a) lines are the best linear fit to the Langmuir model.

3.4.4. Effect of coexisting ions

Generally, Cr(VI)-bearing wastewaters such as chrome-plating wastewater and leather tannery wastewater contain dissolved salts. Thus, the presence of other ions may interfere with Cr(VI) species and influences the adsorption efficiency of the latter ion onto the adsorbent surface [13,36,37]. We voluntarily chosen the NPs with the cobalt composition x ~ 0.6 and the following common coexisting anions and cations: (Cl^-, SO_4^{2-}, NO_3^-, PO_4^{3-}) and (Ni^{2+}, Ba^{2+}, Co^{2+}, Cu^{2+}, Zn^{2+}, Pb^{2+}) to study the effect of the ions on the removal efficiency of Cr(VI) by the NPs. To a mixture of 5 mL 100 mg L^{-1} of each ion and 5 mL 100 mg L^{-1} Cr(VI) was added 20 mg of NPs (2 mg L^{-1}) and then shaken for about 3.0 h. Note that these working concentrations chosen for the common ions (50 mg L^{-1}) are expected to be the maximum concentrations often reached in wastewaters. While, in domestic sewage effluents and in some industrial effluents, sulfate concentration can vary from some hundreds to several thousand mg L^{-1}. Then, the supernatant of each preparation was separated from the Cr(VI)-loaded NPs using a strong magnet and the UV–Vis absorbance of each the solution was measured (Fig. 16). These preparations are denoted as "Cr(VI) + NPs + symbol of coexisting ion", for instance "Cr(VI) + NPs + Pb^{2+}". Note, for comparison, a preparation without a coexisting ion denoted as "Cr(VI) + NPs" was also simultaneously prepared by adding 20 mg of NPs to 10 mL of 50 mg L^{-1} Cr(VI).

The maxima of absorbance of the supernatants lays in both sides of that of the "Cr(VI) + NPs" supernatant (see the zoom-view in the inset of Fig. 16); for instance the absorbance of the supernatants in presence of PO_4^{3-} and SO_4^{2-} ions is higher than that of the supernatant of "Cr(VI) + NPs". While, absorbance of the supernatant in presence of Pb^{2+} ions is noticeably lower than that of the supernatant of "Cr(VI) + NPs"; the yellowish color of the supernatant appears less intense than that of the "Cr(VI) + NPs" preparation with the appearance of a small amount of white precipitate in the bottom of the test tube. Results of Cr(VI) removal efficiency by the NPs in the presence of each of the aforementioned coexisting ions along with the that of the supernatant of "Cr(VI) + NPs" (without coexisting ions) are plotted in Fig. 17.

From the results, a number of interpretations can be made: (i) Except Pb^{2+}, the effect of the coexisting cations (Ni^{2+}, Co^{2+}, Cu^{2+}, Ba^{2+}, Zn^{2+}) on the Cr(VI) removal efficiency by the NPs was rather insignificant. Their influence is less than 5%. The result can be interpreted as follows: at pH ~ 2.0 (far below the pH of the zero point of charge of spinel-type ferrites), the ferrite NPs are positively charged at their surface with the dominant $(OH_2)^+$ entities [38]. While, the Cr(VI) species are negatively charged, and they are predominantly present in the form of $HCrO_4^-$ [38,39]. This leads to an electrostatic repulsion between the NPs surface and the coexisting cations, namely Ni^{2+}, Co^{2+}, Cu^{2+}, Ba^{2+} and Zn^{2+} and favors the immobilization of the Cr(VI) species on the NPs adsorption active sites. (ii) In the case of the coexisting cation Pb^{2+}, the effect on the removal efficiency of Cr(VI) species appeared to be larger than that observed with the free-coexisting ions solution ("Cr(VI) + NPs"). In fact, in acidic aqueous medium, an additional phenomenon happens; Pb^{2+} cations combine with anions in a complete chemical reaction, resulting in the formation of the white precipitate lead chromate according to the following equation [40]:

$$Pb^{2+}(aq) + HCrO_4^-(aq) \rightarrow PbCrO_4(s) + H^+(aq) \quad (12)$$

(iii) The effect of the coexisting anions (Cl^-, SO_4^{2-}, NO_3^-, PO_4^{3-}) on the Cr(VI) removal efficiency by the NPs is negative; the removal efficiency of Cr(VI) onto the NPs surface is less than that observed with the "Cr(VI) + NPs" preparation. The observed results can be explained on the basis on a competitive adsorption of the coexisting anionic species with the Cr(VI) species onto the positively charged NPs surface. Additionally, the removal percentage depends strongly on the type of the anion. The effect of the Cl^- and

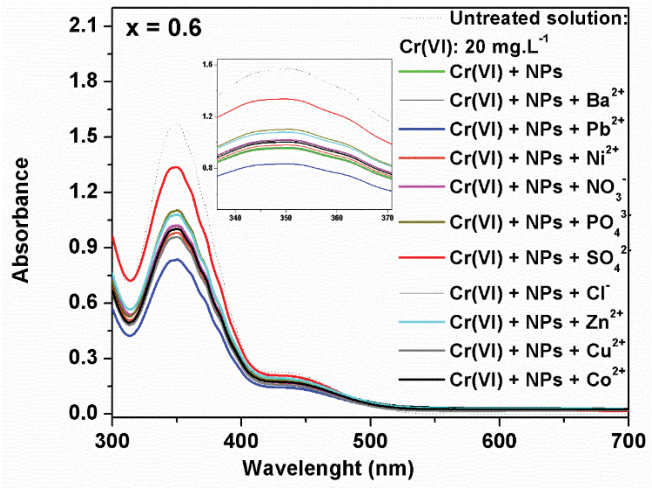

Fig. 16. Absorbance spectra of supernatants of a mixture of Cr(VI) solutions (5 mL; 50 mg L^{-1}) and a variety of coexisting ions solutions (5 mL; 50 mg L^{-1}) in the presence of the NPs with x ~ 0.6 and the dose of 2.0 g L^{-1}.

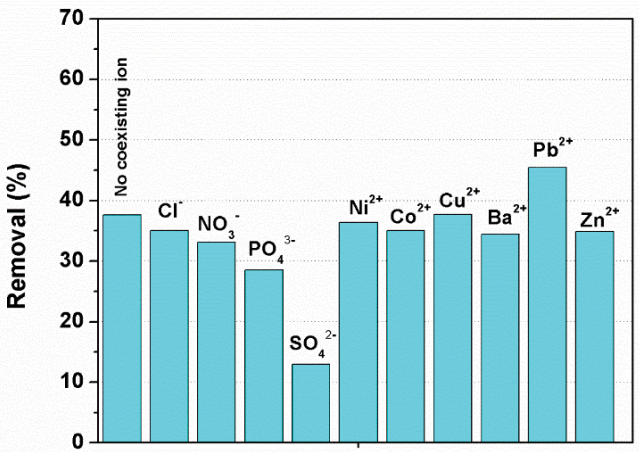

Fig. 17. Effect of coexisting ions on the sorption efficiency of Cr(VI) solutions (5 mL; 50 mg L^{-1}) in the presence of a variety of coexisting ions solutions (5 mL; 50 mg L^{-1}) and a NPs (x ~ 0.6) dose of 2.0 g L^{-1}.

NO_3^- species did not alter significantly the Cr(VI) sorption behavior. This observation is consistent with other studies that found negligible effects of these ions on Cr(VI) removal by spinel-type ferrite NPs [39]. Compared with Cr(VI) species, nitrate and chloride ions are poor ligands and suggest a weaker adsorption mechanism via complexation. Even at higher concentrations (much larger than 50 mg L^{-1}) (not shown), no significant competitive influence on Cr(VI) from these ions was observed. The effect of phosphate (PO_4^{3-}) and sulfate (SO_4^{2-}) ions is remarkable with a more pronounced effect in the case of sulfate ions. Surface complexation may be the main cause for the reduced removal of Cr(VI) in the presence of phosphate and sulfate species [13]. At pH ~ 2.0, as mentioned before, the NPs are positively charged at their surface. While, the Cr(VI), the phosphate and the sulfate species are negatively charged. The latter two ions are predominantly in the form of $H_2PO_4^-$ and SO_4^{2-}, respectively. All the three anions are expected to be strongly attracted to the NPs surface via electrostatic interactions. Therefore, $H_2PO_4^-$ and SO_4^{2-} could potentially compete with the hexachromium anion, resulting in less immobilization on the sorption sites on the NPs surface. The phosphatation is likely occurring through the interaction of $H_2PO_4^-$ entities with Fe^{3+} in octahedral sites of the ferrite NPs with formation of monoprotonated binuclear species [41]. Other studies have shown similar trends but with a less influence of the competition ions in the case of our NPs [13,36,42]. Saidur et al. [13] reported that the presence of PO_4^{3-} significantly lowers the ability of the NPs of commercially mixed magnetite-maghemite NPs to remove Cr(VI) and the effect increases with increasing phosphate concentration. For instance, for a fixed NPs dose of 0.4 g L^{-1}, the removal efficiency is of about 50% and 80% PO_4^{3-} concentration of 4 and 12 mg L^{-1}, respectively. The SO_4^{2-} ions inhibited the removal efficiency much greater possibly due to the formation of $FeSO_4^+$ complex at the NPs surface which is at its maximum stability at pH around 2.0 and at a SO_4^{2-} to Fe^{3+} molar ratio higher than the unity [43].

3.5. Recycling study

Adsorption–desorption–regeneration tests were conducted at pH 2.0 on a mixture of 10 mL Cr(VI) solutions of an initial concentration of 50 mg L^{-1} and 40 mg of NPs (4.0 g L^{-1}). To test the reusability of the nanoadsorbent, the following procedures were followed: (i) the mixture was shaked for 10 min. (ii) The mixture was allowed to stand for about 150 min. (iii) The supernatant was separated from the NPs with the aid of an NdFeB magnet and the absorbance of the solution was measured. (iv) The Cr(VI)-loaded NPs were dispersed in an excess of 0.5 M NaOH (about 30 mL) and then the mixture was sonicated for about 5 min. Clearly, the supernatant shows the characteristic yellow color of an aqueous Cr(VI) solution. The last step was repeated until no detectable Cr(VI) was observed in the washing which can be easily confirmed by UV–visible. (v) The regenerated Cr(VI)-free NPs were washed with ultrapure deionized water under sonication until the pH of the washed water became neutral. (vi) The washed nanoadsorbent was dried at 60°C for about 24 h. to be reused for the subsequent adsorption–desorption–regeneration cycle as described in the procedure above. Seven consecutive cycles of adsorption–desorption–regeneration were carried out to validate the reusability of the produced nanoferrite for the removal of Cr(VI) from an aqueous solution. Fig. 18 shows the removal efficiency and quantity of Cr(VI) during seven cycles of adsorption–desorption–regeneration.

As can be seen, a good reproducibility of the adsorption capacity (mean value ≈ 62, SD < 4) in the adsorption capacity of the nanoadsorbent during the seven cycles was achieved, which meant that there were no irreversible adsorbent sites on the surface of the adsorbent. The experimental results indicated that the studied NPs have an excellent regeneration/reusability, which demonstrates their suitability for the design of a continuous process to remove Cr(VI)-bearing wastewaters.

On comparing the adsorption–desorption performance (kinetics, capacity, reusability, chemical stability) of the produced NPs $Co_x^{2+}Fe_{\frac{8-2x}{3}}^{3+}O_4$ (x ~ 0.6), with other reported magnetically separable spinel-type nanoferrites (Table 4) [15,44–51], one can notice that (i) the NPs have a significant adsorption capacity which is quite comparable with reported adsorption capacities of some other NPs. (ii) $Co_x^{2+}Fe_{\frac{8-2x}{3}}^{3+}O_4$ (x ~ 0.6) NPs exhibit relatively higher saturation magnetization which allowed their ease magnetic separation, (iii) the present NPs are highly recyclable, (iv) in addition to the above comparisons, in case of our NPs, the equilibrium state for the Cr(VI) removal is rapidly reached (less than 30 min).

All the features suggested that our polyol-made NPs are promising adsorbent materials for treatment of Cr(VI)-bearing liquid media. Besides, it is of importance to emphasize that the removal percentage increases with the decrease in Cr(VI) concentration. Thus, for environmental purpose, we can expect that an appropriate adjustment of the dose can reduce the Cr(VI) concentration to the maximum allowable discharge limits of industrial and municipal waste. Environmentally, the allowable Cr(VI) dose depends on the medium in which the waste is discharged. In general, toxicity for most microorganisms occurs in the range of

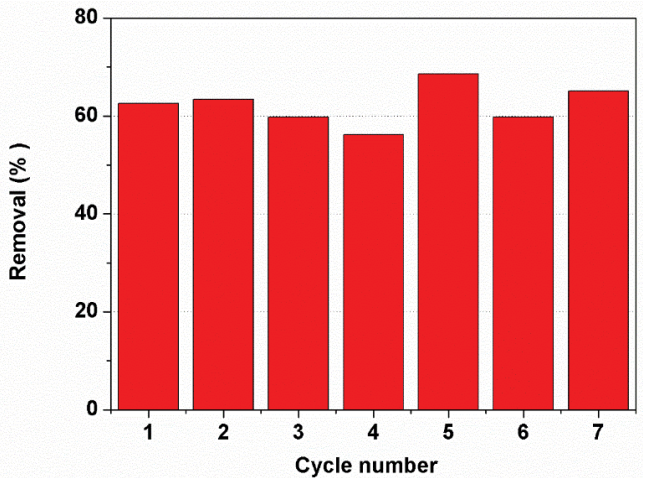

Fig. 18. Reusability of the low-temperature calcined NPs (x ~ 0.6) for the adsorption–desorption–adsorption of Cr(VI) during seven cycles.

Table 4
Comparison of selected characteristics of the present produced spinel-type nanoferrite $Co_x^{2+}Fe_{\frac{8-2x}{3}}^{3+}O_4$ ($x \sim 0.6$) with those of other reported nanoferrites

NPs	Particle size/nm	Saturation magnetization/ emu g^{-1}	pH	Temperature/°C	NPs dose/g L^{-1}	Adsorption capacity for Cr(VI) species	Regeneration efficiency/%, number of cycles	Reference
Fe_3O_4	14.8 (crystallite size)	NA	6.0	Room temperature	1.5	15.4	NA	[44]
Mn_3O_4	~20	NA	3.0	45	2.5	5.8	NA	[45]
γ-Fe_2O_3	~15	67	–	Room temperature	4	12.5	NA	[15]
γ-Fe_2O_3	10	3.3	2.5	25	5	~15	100%, 5 cycles	[46]
$CoFe_2O_4$	12–21	50.8	6.0	55	10	16.7	60%, 5 cycles	[47]
$CoFe_2O_4$/activated carbon composite	–	~7	2.0	25	4	~83	NA	[48]
$MnFe_2O_4$	10	3.6	2.0	25	5	31.5	100%, 6 cycles	[49]
$CuFe_2O_4$	15–20	13	3.0	Room temperature	1.0	9.2	NA	[50]
$NiFe_2O_4$–PANi nanocomposite	NA	NA	2.0	Room temperature	20	~12	NA	[51]
$Co_x^{2+}Fe_{\frac{8-2x}{3}}^{3+}O_4$ ($x \sim 0.6$)	5.2 ± 1.1	69	2.0	Room temperature	4	≈17	~100%, 7 cycles	Present study

NA: Not applicable

0.05–5.0 mg chromium/kg of medium. Some aquatic species are more sensitive and the allowable Cr(VI) dose is less than 0.01 mg L^{-1} [52]. We believe that high reduction of Cr(VI) concentration could be achieved performing subsequent treatment of Cr(VI)-bearing wastewaters in a cascade system of a combined magnetic NPs beds/magnetic flow-based technique appropriately installed in the flow effluent.

4. Conclusion

The present study provides a clear determination of the effect of several physicochemical parameters on the removal efficiency of hexavalent chromium from synthetic wastewaters by novel superparamagnetic cobalt ferrite NPs produced by the polyol method. The Cr(VI) removal efficiency was found to be strongly dependent on both intrinsic (NPs size, cobalt composition,…) and extrinsic (nanoadsorbent dosage, contact time,…) parameters. Thanks to the reasonable magnetic properties and the ultrafine nature of the produced NPs, very fast removal rate with a reasonable removal percentage was achieved. Among all tested kinetic models, the pseudo-second-order model fits the kinetic data. While, the adsorption isotherms fitted better to Langmuir model, which means that the Cr(VI) entities were dominated by monolayer adsorption process. The effect of the coexisting ions Ni^{2+}, Co^{2+}, Cu^{2+}, Ba^{2+}, Zn^{2+}, Cl^-, NO_3^- on the removal of Cr(VI) on the NPs with the cobalt composition $x \sim 0.6$ was insignificant. While, SO_4^{2-}, PO_4^{3-} and Pb^{2+} ions exhibited noticeable negative and positive effect, respectively. Additionally, the adsorbent was successfully recycled seven times without noticeable reduction of the removal efficiency of Cr(VI) species. Based on these findings, we conclude that from purification applications (low concentrated medium) point of view, a high removal percentage of Cr(VI) can be achieved. In the case of relatively concentrated Cr(VI) aqueous media (municipal and industrial wastewaters), consecutive treatment of the Cr(VI)-bearing effluents may be achieved on a system of a combined magnetic NPs beds with a magnetic flow-based technique, thus leading to environmentally allowable limits Cr(VI)-bearing discharges.

Acknowledgment

The authors are greatly indebted to the deanship of Scientific Research at Northern Border University for its funding of the present research work through the research project No. 7259-SCI-2017-1-8-F.

References

[1] C.J. Vörösmarty, P.B. McIntyre, M.O. Gessner, D. Dudgeon, A. Prusevich, P. Green, S. Glidden, S.E. Bunn, C.A. Sullivan, C. Reidy Liermann, P.M. Davies, Global threats to human water security and river biodiversity, Nature, 467 (2010) 555–561.
[2] F. Denisa, F. Anton, A. Ecaterina, Recent Advances in Using Magnetic Materials for Environmental Applications, Chapter 1, M.G. Alexandru, Ed., Water Purification, Vol. 9, Academic Press, An imprint of Elsevier, United States, 2017, pp. 1–32.
[3] M. Barbosa, N.F.F. Moreira, A.R. Ribeiro, M.F.R. Pereira, A.M.T. Silva, Occurrence and removal of organic micropollutants: an overview of the watch list of EU Decision 2015/495, Water Res., 94 (2016) 257–279.
[4] World Water Assessment Programme (UNESCO WWAP), 2017.

[5] K.R. Kunduru, M. Nazarkovsky, S. Farah, R.P. Pawar, A. Basu, A.J. Domb, Nanotechnology for Water Purification: Applications of Nanotechnology Methods in Wastewater Treatment, Chapter 2, M.G. Alexandru, Ed., Water Purification, Vol. 9., Academic Press, An imprint of Elsevier, 2017, United States, pp. 33–74.
[6] B. Marek, K. Nalan, L.R. Bernabé, B. Jochen, Series: Sustainable Water Developments, Vol. 2, Innovative Materials and Methods for Water Treatment: Solutions for Arsenic and Chromium Removal, CRC Press/Balkema, Taylor & Francis, United States, 2016.
[7] X. Qu, P.J.J. Alvarez, Q. Li, Applications of nanotechnology in water and wastewater treatment, Water Res., 47 (2013) 3931–3946.
[8] C. Dai, Y. Zhou, H. Peng, S. Huang, P. Qin, J. Zhang, Y. Yang, L. Luo, X. Zhang, Current progress in remediation of chlorinated volatile organic compounds: a review, J. Ind. Eng. Chem., 62 (2018) 106–119.
[9] G. Jiang, M. Lan, Z. Zhang, X. Lv, Z. Lou, X. Xu, F. Dong, S. Zhang, Identification of Active Hydrogen Species on Palladium Nanoparticles for an Enhanced Electrocatalytic Hydrodechlorination of 2,4-Dichlorophenol in Water, Environ. Sci. Technol., 51 (2017) 7599–7605.
[10] C. Grégorio, L. Eric, D.W. Lee, M.C. Nadia, Conventional and non-conventional adsorbents for wastewater Treatment, Environ. Chem. Lett., 17 (2019) 195–213.
[11] I. Ali, New generation adsorbents for water treatment, Chem. Rev., 112 (2012) 5073–5091.
[12] R. Shalini, U.P. Charles Jr., M. Dinesh, Magnetic magnetite (Fe_3O_4) nanoparticle synthesis and applications for lead (Pb^{2+}) and chromium (Cr^{6+}) removal from water, J. Colloid Interface Sci., 468 (2016) 334–346.
[13] S.R. Chowdhury, E.K. Yanful, Arsenic and chromium removal by mixed magnetite-maghemite nanoparticles and the effect of phosphate on removal, J. Environ. Manage., 91 (2010) 2238–2247.
[14] G. Fei, M.L. Meng, Y. Hui, X.Z. Bao, Effective removal of heavy metal ions $Cd^{2+,}$ Zn^{2+}, Pb^{2+}, Cu^{2+} from aqueous solution by polymer-modified magnetic nanoparticles, J. Hazard. Mater., 211–212 (2012) 366–372.
[15] L.B. Tahar, M.H. Oueslati, M.J.A. Abualreish, Synthesis of magnetite derivatives nanoparticles and their application for the removal of chromium (VI) from aqueous solutions, J. Colloid Interface Sci., 512 (2018) 115–126.
[16] L.B. Tahar, M.H. Oueslati, G. Bilel, A Comparative study of two new CoZn nanoferrites: characterization, magnetic properties, and efficiency for the removal of hexavalent chromium from wastewaters, Desal. Wat. Treat., 144 (2019) 243–256.
[17] X'Pert HighScore Plus, V 2.0, PANalytical B.V. Almelo, The Netherlands, 2003.
[18] G.K. Williamson, W.H. Hall, X-ray line broadening from filed aluminum and wolfram, Acta Metall., 1 (1953) 22–31.
[19] J. Smit, H.P.J. Wijn, Ferrites, Philips Technical Library, Netherlands, 1959.
[20] L.B. Tahar, H. Basti, F. Herbst, L.S. Smiri, J.P. Quisefit, N. Yaacoub, J.M. Grenèche, S. Ammar, $Co_{1-x}Zn_xFe_2O_4$ ($0 \le x \le 1$) nanocrystalline solid solution prepared by the polyol method: characterization and magnetic properties, Mater. Res. Bull., 47 (2012) 2590–2598.
[21] H.S.C. O'Neill, A. Navrotsky, Simple spinels: crystallographic parameters, cation radii, lattice energies, and cation distribution, Am. Mineral., 68 (1983) 181–194.
[22] R.D. Waldron, Infrared spectra of ferrites, Phys. Rev., 99 (1955) 1727–1735.
[23] H. Basti, L.B. Tahar, L.S. Smiri, F. Herbst, M.-J. Vaulay, F. Chau, S. Ammar, S. Benderbous, Catechol derivatives-coated Fe_3O_4 and γ-Fe_2O_3 nanoparticles as potential MRI contrast agents, J. Colloid Interface Sci., 341 (2010) 248–254.
[24] D. Makovec, M. Drofenik, Non-stoichiometric zinc-ferrite spinel nanoparticles, J. Nanopart. Res., 10 (2008) 131–141.
[25] M. Artus, L.B. Tahar, F. Herbst, L. Smiri, F. Villain, N. Yaacoub, J.M. Grenèche, S. Ammar, F. Fiévet, Size-dependent magnetic properties of $CoFe_2O_4$ nanoparticles prepared in polyol, J. Phys. Condens. Matter., 23 (2011) 506001 (9pp).
[26] D. Cangussu, W.C. Nunes, H.L. da Silva Corrêa, W.A. de Almeida Macedo, M. Knobel, O.L. Alves, A.G.S. Filho, I.O. Mazali, γ-Fe_2O_3 nanoparticles dispersed in porous Vycor glass: a magnetically diluted integrated system, J. Appl. Phys., 105 (2009) 013901 (9pp).
[27] J.M. Vargas, L.M. Socolovsky, M. Knobel, D. Zanchet, Dipolar interaction and size effects in powder samples of colloidal iron oxide nanoparticles, Nanotechnology, 16 (2005) 285–290.
[28] J.P. Chen, C.M. Sorensen, K.J. Klabunde, G.C. Hadjipanayis, E. Devlin, A. Kostikas, Size-dependent magnetic properties of $MnFe_2O_4$ fine particles synthesized by coprecipitation, Phys. Rev. B: Condens. Matter, 54 (1996) 9288–9296.
[29] D. Zhang, K.J. Klabunde, C.M. Sorensen, G.C. Hadjipanayis, Magnetization temperature dependence in iron nanoparticles, Phys. Rev. B: Condens. Matter, 58 (1998) 14167–14170.
[30] L. Chao, J.R. Adam, Z.J. Zhang, Synthesis of magnetic spinel ferrite $CoFe_2O_4$ nanoparticles from ferric salt and characterization of the size-dependent superparamagnetic properties, Pure Appl. Chem., 72 (2000) 37–45.
[31] S. Qing, Z.J. Zhang, Correlation between spin-orbital coupling and the superparamagnetic properties in magnetite and cobalt ferrite spinel nanocrystals, J. Phys. Chem. B, 110 (2006) 11205–11209.
[32] R. Gong, J. Ye, W. Dai, X. Yan, J. Hu, S. Li, H. Huang, Adsorptive removal of methyl orange and methylene blue from aqueous solution with finger-citron-residue-based activated carbon, Ind. Eng. Chem. Res., 52 (2013) 14297–14303.
[33] Y.S. Ho, G. McKay, Pseudo-second-order model for sorption processes, Process Biochem., 34 (1999) 451–465.
[34] I. Langmuir, The adsorption of gases on plane surfaces of glass, mica and platinum, J. Am. Chem. Soc., 40 (1918) 1361–1403.
[35] H.M.F. Freundlich, Über die adsorption in lösungen, Ind. Eng. Chem. Fundam., 57 (1906) 385–470.
[36] A.B. Ali, A. Mehdi, G. Gholamreza, N. Jaafarzadeh, B. Zeynab, Adsorption of chromium(VI) from saline wastewater using spent tea-supported magnetite nanoparticle, Desal. Wat. Treat., 57 (2016) 1–13.
[37] G. Dönmez, Z. Aksu, Removal of chromium(VI) from saline wastewaters by *Dunaliella* species, Process Biochem., 38 (2002) 751–762.
[38] A.H. Meena, Y. Arai, Effects of common groundwater ions on chromate removal by magnetite: importance of chromate adsorption, Geochem. Trans., 17 (2016) 1–13.
[39] H. Jing, C. Guohua, M.C.L. Irene, Removal and recovery of Cr(VI) from wastewater by maghemite nanoparticles, Water Res., 39 (2005) 4528–4536.
[40] P.H. Riege, Electrochemistry, Springer Science & Business Media, 1994, p. 177.
[41] T.J. Daou, S. Begin-Colin, J.M. Grenèche, F. Thomas, A. Derory, P. Bernhardt, P. Legaré, G. Pourroy, Phosphate adsorption properties of magnetite-based nanoparticles, Chem. Mater., 19 (2007) 4494–4505.
[42] W. Zhang, P. Singh, E. Paling, S. Delides, Arsenic removal from contaminated water by natural iron ores, Miner. Eng., 17 (2004) 517–524.
[43] W.T. Dudley, M.T. Norhayati, The influence of a smectite clay on the hydrolysis of iron(III), Colloids Surf., 60 (1991) 369–398.
[44] S. Asuha, B. Suyala, S. Zhao, Porous structure and Cr(VI) removal abilities of Fe_3O_4 prepared from Fe–urea complex, Mater. Chem. Phys., 129 (2011) 483–487.
[45] Y. Cantu, A. Remes, A. Reyna, D. Martinez, J. Villarreal, H. Ramos, S. Trevino, C. Tamez, A. Martinez, T. Eubanks, J.G. Parsons, Thermodynamics, kinetics, and activation energy studies of the sorption of chromium(III) and chromium(VI) to a Mn_3O_4 nanomaterial, Chem. Eng. J., 254 (2014) 374–383.
[46] J. Hu, G. Chen, I.M.C. Lo, Selective removal of heavy metals from industrial wastewater using maghemite nanoparticle: performance and mechanisms, J. Environ. Eng., 132 (2006) 709–715.
[47] V. Srivastava, T. Kohout, M. Sillanpää, Potential of cobalt ferrite nanoparticles ($CoFe_2O_4$) for remediation of hexavalent chromium from synthetic and printing press wastewater, J. Environ. Chem. Eng., 4 (2016) 2922–2932.

[48] W. Qiu, D. Yang, J. Xu, B. Hong, H. Jin, D. Jin, X. Peng, J. Li, H. Ge, X. Wang, Efficient removal of Cr(VI) by magnetically separable $CoFe_2O_4$/activated carbon composite, J. Alloys Compd., 678 (2016) 179–184.
[49] J. Hu, I.M. Lo, G. Chen, Fast removal and recovery of Cr(VI) using surface-modified jacobsite ($MnFe_2O_4$) nanoparticles, Langmuir, 21 (2005) 11173–11179.
[50] P.L. Hariani, F. Riyanti, Magnetic $CuFe_2O_4$ nanoparticles for adsorption of Cr(VI) from aqueous solution, Adv. Mater. Res., 896 (2014) 104–107.
[51] S. Agrawal, N.B. Singh, Removal of toxic hexavalent chromium from aqueous solution by nickel ferrite-polyaniline nanocomposite, Desal. Wat. Treat., 57 (2016) 17757–17766.
[52] European Commission DG ENV, E3 Project ENV.E.3/ETU/2000/0058, Heavy Metals in Waste Final Report, February 2002.